Refraction of the M$_2$ internal tides by mesoscale eddies in the South China Sea

Zheng Guo [a], Shuya Wang [b], Anzhou Cao [c,b,*], Jieshuo Xie [d,e], Jinbao Song [c], Xinyu Guo [b]

[a] *Marine Science and Technology College, Zhejiang Ocean University, Zhoushan, China*
[b] *Center for Marine Environmental Studies, Ehime University, Matsuyama, Japan*
[c] *Ocean College, Zhejiang University, Zhoushan, China*
[d] *State Key Laboratory of Tropical Oceanography, South China Sea Institute of Oceanology, Chinese Academy of Sciences, Guangzhou, China*
[e] *Southern Marine Science and Engineering Guangdong Laboratory (Guangzhou), Guangzhou, China*

A B S T R A C T

Mesoscale eddies (MEs) are active in the northern South China Sea, yet it is hard to separate their impacts on the internal tides (ITs) from those of other subtidal circulation. This study examines the role of an anticyclonic eddy and a cyclonic eddy in modulating the M$_2$ ITs based on numerical simulations. In idealized experiments, MEs that differ only in polarity are located on the main beam of the M$_2$ ITs in the northern South China Sea. Results show that the anticyclonic eddy and cyclonic eddy cause northward and southward refractions of the M$_2$ ITs, respectively, which echoes the realistic simulation. The most dramatic changes in the M$_2$ IT energy fluxes occur on the continental slope to the west of the MEs. Theoretical analysis based on the ray-tracing model and the empirical model for estimating wave front locations reveals that the MEs cause refraction of the M$_2$ ITs by changing the phase speeds. Further investigation shows that the currents related to the MEs make a greater contribution to the IT refraction than the ME-associated stratification. These results have important implications for investigation of spatial and temporal variations in the magnitude and direction of the M$_2$ IT energy fluxes.

1. Introduction

Internal tides (ITs) are ubiquitous in the stratified ocean. As an intermediate step of the tides-to-turbulence cascade, ITs contribute greatly to dissipating surface tidal energy and enhancing mixing (Rudnick et al., 2003). ITs are generated in stratified waters by the interaction of barotropic tidal currents with variable bottom topographies (Garrett and Kunze, 2007) and could propagate thousands of kilometers away from their generation site (Zhao, 2014). In this process, ITs inevitably interact with other oceanic flows and processes, such as the wind-driven circulations and mesoscale eddies (MEs). The modification of ITs by MEs has been an ongoing subject of study.

MEs can impact the radiation of ITs as they are associated with varying stratification and sheared currents. Previous oceanic observations showed direct evidence for the interaction between ITs and MEs. Chavanne et al. (2010) found that in the Kauai Channel, Hawaii, the cyclonic eddy caused the energy of IT rays propagating through its core to increase near the surface (up to a factor of 15), with surfacing time delayed by up to 5 h (~150° phase lag). Liang (2014) suggested that the variation of baroclinic semidiurnal tides over the East Pacific Rise was related to the eddy-induced low-frequency flows in the deep ocean, particularly their cross-ridge components. In the Atlantic Ocean, Löb

et al. (2020) noticed a pronounced damping of the semidiurnal IT energy fluxes coinciding with the passing of two eddies. In the presence of a surface-intensified eddy, the coherent part of the IT in the first two modes was lowered. However, a subsurface eddy caused decease of IT energy flux mainly in the second mode. Whereas, due to the temporal and spatial limitation, it is hard to figure out the dominant mechanism on how MEs affect the ITs directly from observations.

For the interpretation of observational results, theoretical models are developed by researchers. The ray tracing model of Rainville and Pinkel (2006) could explain the refraction of ITs through a barotropic mesoscale current field. Duda et al. (2018) improved that ray tracing model by using extended Jones equation and considering anisotropism of wave speed. Their results indicated that the IT rays could be strongly redirected and even trapped by baroclinic currents. In addition to the ray tracing model, other theoretical models such as "hydrostatic wave equations" (Wagner et al., 2017) were also established for corresponding investigations. However, it should be noted that approximations are introduced in the above theoretical models. As a result, they may lead to divergent results and still need further modification.

Apart from theoretical models, numerical models are another effective approach for exploring the IT-ME interaction. Compared with theoretical ones, numerical models provide three-dimensional wave

---

fields of ITs without neglecting several terms in the governing equations. Based on idealized experiments, Dunphy and Lamb (2014) showed that hot and cold spots of energy fluxes were produced in beam-like patterns after mode-1 ITs passed through a barotropic eddy. The pass of mode-1 ITs through a mode-1 baroclinic eddy resulted in IT energy transfer to modes two and higher. Ponte and Klein (2015) demonstrated that as ITs propagate across a front, they lose coherence due to the interaction with eddies generated by the unstable jet. By using realistic topography and forcing, numerical models could also reproduce the radiation of ITs in an eddying field for specific regions. Corresponding results revealed that mesoscales eddies result in time-variable refraction of ITs and hence the variation of IT energy (Zaron and Egbert, 2014; Varlamov et al., 2015; Savage et al., 2020).

In the South China Sea (SCS), both the ITs and MEs are active. The SCS has been identified as a site of intense ITs due to the double meridional submarine ridges, strong stratification, and astronomical tides at the Luzon Strait (LS). The evolution of ITs in the SCS has been explored widely (e.g., Xu et al., 2016; Wang et al., 2021). They are generated at the LS, propagate westward in the deep central basin, and then shoal onto the continental slope (Alford et al., 2015). At each stage of their evolution, ITs are susceptible to MEs that are frequent and energetic in the SCS. Altimetric observation reveals that MEs are present in the northern SCS during 35%–60% of the time (Chen et al., 2011). The low-frequency current related to the MEs could reach 1 m/s at the surface and the temperature anomaly resulting from anticyclonic eddies (AE) and cyclonic eddies (CE) near the main thermocline are up to 7.5 °C and −3.0 °C, respectively (Zhang et al., 2013). Consequently, inevitable modulation of ITs by MEs in the SCS deserves attention. Hydrographic observations reveal the changes in propagation speed and the energy refraction of the mode-1 semidiurnal ITs, as well as strengthened mode-2 ITs when a pair of eddies passed the northern SCS (Huang et al., 2018). However, because the Kuroshio is strong and takes variable intrusive pathways within the LS (Nagai et al., 2019), its influence on the ITs in the SCS can't be ignored (Kerry et al., 2014; Xu et al., 2021; Cao et al., 2022) but it is hard to be separated from the influence of MEs. Separately investigating the influence of MEs is the motivation for our study.

In this study, the influence of MEs on the M_2 IT refraction in the northern SCS is numerically investigated with specially designed realized and idealized experiments. The configuration for both realized and idealized experiments as well as the analysis methods are presented in Section 2. In Section 3, the responses of the M_2 ITs to a pair of eddies (an AE and a CE) are first simulated in the real context where the Kuroshio and other subtidal circulation remains. To exclude the influence of the Kuroshio and other subtidal circulation and quantify the influence of the MEs, a series of idealized experiments are conducted. In Section 4, theoretical analysis is performed based on the ray-tracing model and the empirical model for estimating wave front. The conclusions summarize the paper in Section 5.

2. Methodology

2.1. CROCO model configurations

2.1.1. Common settings

This study employs the Coastal and Regional Ocean COmmunity (CROCO) model (version 1.0; www.croco-ocean.org) to explore the impacts of MEs on the M_2 ITs in the northern SCS. The CROCO model is built on the regional ocean modelling system from Institut de Recherche pour le Developpement (ROMS_AGRIF) and, by default, solves the primitive equations under the hydrostatic equilibrium and Boussinesq approximation. The model performs well in different scenarios including the ITs in the northern SCS (Marchesiello et al., 2019; Renault et al., 2017; Guo et al., 2020a; 2020b; 2021; Cao et al., 2022). Since the horizontal scale of ITs is much larger than the vertical scale in the deep water of the northern SCS (Zhao, 2014; Xu et al., 2016), and breaking of

ITs and other non-hydrostatic processes are not our focus, the hydrostatic approximation is valid for this study.

The domain of simulation covers the northern SCS and part of the Western Pacific with the LS located in the center (Fig. 1). The model has a uniform horizontal resolution of $1/20°$ (approximately 5 km) and 25 uneven vertical sigma layers with a higher resolution near the surface and bottom. The topography used in the simulation is extracted from the 1-min gridded elevations/bathymetry for the world (ETOPO1) data (NOAA National Geophysical Data Center, 2009) and has been smoothed to minimize the horizontal pressure gradient errors. The M_2 tidal forcing is introduced into the model at the open boundaries with surface elevations and barotropic currents extracted from Oregon State University global models of ocean tides (TPXO7.2; Egbert and &Erofeeva, 2002). A ten-cell-wide (0.5°) sponge layer is used to absorb the baroclinic energy to avoid artificial reflection of ITs at the open boundaries. The Large-McWilliams-Doney k-profile parameterization mixing scheme (Large et al., 1994) is used for vertical turbulent mixing of momentum and tracers. The Laplacian horizontal mixing of momentum is used for the subgrid-scale turbulence.

2.1.2. Realized experiments

In the realized experiment, we simultaneously simulate the M_2 ITs and subtidal circulation including MEs and the Kuroshio. The boundary and initial conditions including temperature, salinity, sea surface height and background currents from the HYbrid Coordinate Ocean Model (HYCOM) are downloaded from the Asia-Pacific Data-Research Center (apdrc.soest.hawaii.edu/data/data.php). The atmospheric forcing is provided by the National Centers for Environmental Prediction Climate Forecast System Version 2 data (https://cfs.ncep.noaa.gov/).

The simulation is integrated for 57 days, from 6 December 2013 to 31 January 2014, when an AE and a CE passed the simulation domain successively. Detailed description of the eddy evolution can be found in Zhang et al. (2016). The simulated results are output every 1 h. The first 10 days are excluded from analysis to ensure that the ITs are sufficiently developed.

To validate the simulated results, the subtidal motions are extracted with a fourth-order lowpass Butterworth filter. The cutoff frequency is set as 0.5 cpd, which is wide enough to extract the background currents and narrow enough to remove higher-frequency signals such as tides (Zhang et al., 2016; Cao et al., 2022). The surface velocity averaged for the entire simulation period is similar to the altimetry observation, and the characteristics of the mean meridional background currents, temperature, and salinity along 22°N are consistent with those of the
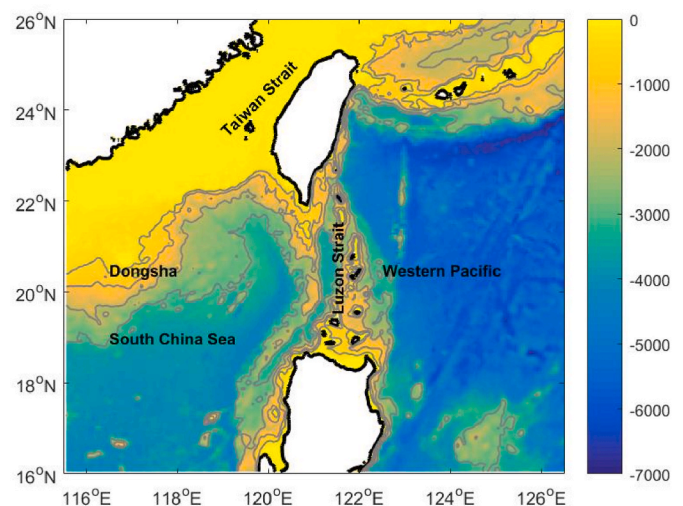

Fig. 1. Bathymetry (shading, unit: m) in the northern SCS, with gray contours indicating −3000, −2000, −1000, and −500 m isobaths.

climatological mean observations in winter (Rudnick et al., 2011, Fig. 4 therein). The M_2 barotropic tide extracted from the model output is also validated by comparing with the TPXO7.2. Details can be found in the supporting information.

2.1.3. Idealized experiments

Since MEs are hard to be separated from the Kuroshio and other subtidal circulation in the real experiments, we conduct three idealized experiments: no-eddy experiment, AE experiment, and CE experiment. In each experiment, the M_2 constituent is introduced at the open boundaries. For the no-eddy experiment, a horizontally homogenous stratification is specified. The stratification is calculated with annual temperature and salinity from the World Ocean Atlas 2009 (WOA09) and averaged over the domain. In the experiments with eddies, the domain is initialized with a single isolated eddy (Dunphy and Lamb, 2014; Xie et al., 2015). The eddy centered at (x_c, y_c) is prescribed by the stream function

$$\Psi(r,z)=\psi(r)\Phi(z)=-\frac{5^{\frac{5}{2}}}{64}U_E L_E \ \text{sech}^4\left(\frac{r}{L_E}\right)\Phi(z) \tag{1}$$

where $r=[(x\text{-}x_c)^2+(y\text{-}y_c)^2]^{1/2}$ is the distance away from the eddy center, $\psi(r)$ is the horizontal structure of the eddy, and $\Phi(z)$ prescribes the vertical structure. The scaling factor of $-5^{5/2}/64$ ensures that $\psi(r)$ yields a peak azimuthal velocity of U_E at $r=L_E\tanh^{-1}(5^{1/2}/5)\approx0.48L_E$. The parameter L_E is the length scale of the eddy, and the peak velocity has dropped to below 2% at a radial distance of $2L_E$. $\Phi(z)$ is composed of solutions to the Sturm-Liouville problem (Michael Dunphy, 2014)

$$\frac{d\Phi_n(z)}{dz^2}+|\mathbf{k}|^2\left(\frac{N^2(z)}{\omega^2-f^2}\right)\Phi_n(z)=0 \tag{2}$$

subject to the boundary conditions

$$\Phi_n(0)=\Phi_n(-H)=0 \tag{3}$$

where $\mathbf{k}=(k, l)$ is the horizontal wave number, N is the buoyancy frequency that represents the stratification, ω is the frequency of the M_2 tide, f is the Coriolis frequency, and H is the total water depth. A numerical method is used for the general $N(z)$ prescribed in this study (Cao et al., 2015). The initial horizontal velocities are $(u, v)=(-\Psi_y, \Psi_x)$, and the density field is prescribed by cyclo-geostrophic and hydrostatic balances. Based on the characteristics of the pair of eddies in the real experiments, the eddy center (x_c, y_c) is set at (119°E, 21°N), $|U_E|$ is 0.9 m/s, L_E is 1×10^5 m, and the eddy is composed of the first baroclinic mode and a barotropic mode such that the velocity is zero at the bottom level. Each idealized experiment is run for 15 days and the results are stored every 1 h. Only the results of the last 5 days are used for analysis.

2.2. Analysis methods for baroclinic tidal energetics

The barotropic-to-baroclinic energy conversion rate E_{bt2bc} is calculated with the pressure perturbation and the vertical barotropic velocity at the seafloor:

$$E_{bt2bc}(t)=p^{'}(-H,t)w_{bt}(-H,t)=p^{'}(-H,t)[\mathbf{u}_{bt}(-H,t)\cdot\nabla(-H)] \tag{4}$$

where t is the time, p' is the pressure perturbation, w_{bt} and $\mathbf{u}_{bt}$ are the vertical and horizontal barotropic velocities. According to Nash et al. (2005), p' is calculated as

$$p^{'}(z,t)=p_{surf}(t)+\int_z^\eta \rho^{'}(\widehat{z},t)g d\widehat{z} \tag{5}$$

where z is the depth, η is water elevation at the surface, ρ' is the density perturbation, g is the acceleration due to gravity, and p_{surf} is the surface pressure, which is determined by

$$\frac{1}{H+\eta}\int_{-H}^\eta p^{'}(z,t)dz=0 \tag{6}$$

The tidal-period-averaged conversion rate is obtained following Zilberman et al. (2011):

$$\langle E_{bt2bc}\rangle=0.5P^{'}(-H)W_{bt}(-H)\cos(\theta_p-\theta_w) \tag{7}$$

where P' (W_{bt}) and θ_p (θ_w) are the amplitude and phase of the pressure perturbation (vertical barotropic velocity) at the seafloor of the M_2 ITs, respectively.

The depth-integrated baroclinic energy flux $\mathbf{F}_{bc}$ is calculated following Kerry et al. (2014, 2016):

$$\mathbf{F}_{bc}=\int_{-H}^\eta p^{'}(z,t)\mathbf{u}^{'}(z,t)dz \tag{8}$$

where $\mathbf{u}'$ is the horizontal baroclinic velocity obtained by

$$\mathbf{u}^{'}(z,t)=\mathbf{u}(z,t)-\overline{\mathbf{u}}(z)-\overline{\mathbf{u}}_0(t) \tag{9}$$

where the three terms on the right-hand side are instantaneous, time-averaged, and depth-averaged horizontal velocities, respectively.

2.3. Calculation of phase speed

We calculate the eigenspeed c_n using the Taylor-Goldstein equation as in Xu et al. (2021):

$$\frac{d^2\widehat{w}}{dz^2}+\left[\frac{N^2}{(U-c_n)^2}-|\mathbf{k}|^2-\frac{d^2U/dz^2}{U-c_n}\right]\widehat{w}=0 \tag{10}$$

where $\widehat{w}$ is the eigenfunction of vertical velocity, and U is the background flow component parallel to the IT direction. Thereafter, the phase speed c_p can be derived from the eigenspeed following Zhao et al. (2010).

$$c_p=\frac{\omega}{(\omega^2-f^2)^{1/2}}c_n \tag{11}$$

In the calculation, if U is set to be zero, c_p would be determined by N. In other words, we exclude the effects of background current and obtain a solution under the sole influence of stratification. If N is set to be horizontally homogenous, the spatial mean stratification of the northern SCS in our case, then we obtain the solution only determined by the background current. In the following, we use the phase speed of the first mode to calculate the wave path, considering that most of the IT energy is transported away by the first mode (Zhao, 2014).

2.4. Energy ray-tracing model

The ray trajectories of the M_2 ITs are calculated following Duda et al. (2018):

$$\begin{cases} \dfrac{dx}{ds}=Q\left[S(\alpha)\cos\alpha+\sin\alpha\dfrac{\partial S}{\partial\theta}\bigg|_{\theta=\alpha}\right] \\ \dfrac{dy}{ds}=Q\left[S(\alpha)\sin\alpha-\cos\alpha\dfrac{\partial S}{\partial\theta}\bigg|_{\theta=\alpha}\right] \\ \dfrac{dp_x}{ds}=QS(\alpha)\dfrac{\partial S}{\partial x} \\ \dfrac{dp_y}{ds}=QS(\alpha)\dfrac{\partial S}{\partial y} \end{cases} \tag{12}$$

where the coordinates (x, y) define the ray trajectory which has length increment ds; the angle $\alpha=\arctan(p_x/p_y)$ is the direction of a vector normal to the phase front; θ is the angle of the wave vector $\mathbf{k}$; Q is the normalization factor; and $S=\mathbf{k}/\omega$ is the slowness vector.

To examine IT propagation behavior in this study, we first calculate

the phase-speed field using the background current and stratification over the domain. These are obtained by averaging the 50-h CROCO output records starting from Day 11 in each idealized experiment. Thereafter, Equation set (12) are integrated to compute IT ray trajectories with initial α (set to be 180° pointing westward in the SCS).

2.5. Empirical model for estimating wave front locations

The empirical model proposed by Jackson (2009) is used to estimate the IT wave front positions in this study. First, the background current and stratification are extracted by averaging the 50-h CROCO output records starting from Day 11 in idealized experiment and the phase speed of the M₂ IT is calculated following Equations (10) and (11). The next step is to determine the propagation time and propagation path for a wave whose speed varies depending on its location along the propagation path. The problem is solved using the two-dimensional eikonal differential equation

$$\left(\frac{\partial T}{\partial x}\right)^2 + \left(\frac{\partial T}{\partial y}\right)^2 = S^2(x, y) \tag{13}$$

where $T(x, y)$ is the travel time between an origin (x_0, y_0) and location (x, y). Only the positions of the mode-1 IT are calculated for the same reason as that in Section 2.3. The geographic origin for the waves and other settings are the same as those in Jackson (2009).

3. Results

3.1. Realized experiment

The MEs and other subtidal motions are first extracted with a fourth-order lowpass Butterworth filter. The eddy evolution is shown in Fig. 2. On Day 16, an AE was centered at approximately 118.5°E, 21°N with a peak velocity near 1 m/s. Thereafter, it moved westward. A CE appeared at the end of December and gradually developed but the associated currents were slightly weaker than the AE. The successful simulation of the eddy pair enables us to explore the ITs' energetics in respondence to subtidal circulation.

We selected two 50-h time windows starting from Days 16 and 38, respectively, to conduct harmonic analysis on the simulated results to calculate the M₂ tidal conversion rates and energy fluxes. The M₂ conversion integrated within the LS (120°−122.5°E, 18.5°−22°N) during
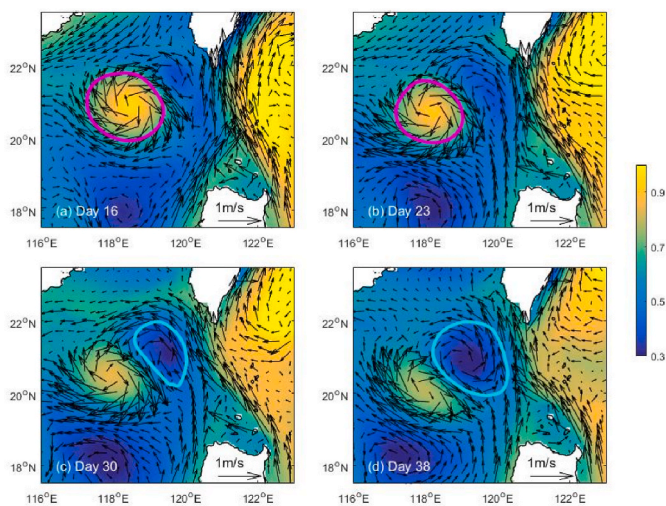

Fig. 2. Evolvement of the subtidal circulation during the simulation period. The surface elevation is indicated by shadings (unit: m) and surface currents by arrows. The magenta and cyan circles indicate locations of the AE and CE nearest to the LS, respectively.

the two periods is approximately 17.52 and 18.07 GW, respectively, which lies within the range (13.01–19.95 GW) estimated by Kerry et al. (2016).

Our focus is then put on the energy fluxes of ITs in the northern SCS where the AE and CE appeared. The propagation of ITs changes in respondence to the MEs (Fig. 3). The M₂ ITs propagated from LS to the SCS in two beams and the north beam bifurcated to some extent upon leaving LS and merged again after reaching 119°E. On Day 16 when an AE was located to the west of the LS, the north beam propagated northwestward after passing the eddy center and impinged on the continental slope at latitudes north of 21°N. However, on Day 38 when the AE was replaced by a CE, the north beam refracted south, directing due west along 21°N. The different patterns indicate refraction of M₂ IT energy by the eddies, which is consistent with observations from moorings (Huang et al., 2018).

The changes of ITs are certainly related to the MEs. However, variation occurring at the IT generation site and before ITs encounter the eddies can also be attributed to the Kuroshio and other background circulation (Kerry et al., 2014; Song and Chen, 2020; Xu et al., 2021; Cao et al., 2022). It is hard to separate and quantify their contribution in the real context. In addition, the AE and CE also differed in positions and strengths. To determine to what extent the polarity of MEs account for the above changes in ITs, we conduct idealized experiments and analyze the results in Section 3.2.

3.2. Idealized experiments

A time window of 50 h starting from Day 11 is selected to calculate the M₂ energy fluxes in each experiment. The start date of the time window ensures that the IT field has well developed and its length ensures that the background field changes very slightly. The background fields in the AE and CE experiments on Day 11 are shown in Fig. 4. Compared to their initial state, both the AE and CE moved a bit westward and their peak velocity showed some decrease. But the two eddies were still quite similar except having different polarity.

The results of no-eddy experiment serve as the benchmark. The M₂ tidal conversion integrated around the LS is 18.52 GW, and the energy propagating into the SCS (5.07 GW) is a bit larger than that into the Western Pacific (4.60 GW). The energy budgets are largely consistent with previous studies (Kerry et al., 2013; Xu et al., 2016). Fig. 5a shows a strong westward beam of the M₂ ITs pointing to the Dongsha Island and a much weaker beam propagating southwestward to the SCS basin. The patterns are generally consistent with previous research (e.g., Kerry et al., 2013; Xu et al., 2016; Zhao, 2020).

The M₂ energy flux beam pointing to the Dongsha Island is stronger than that propagating southwestward and the eddy is located just on its path. Consequently, focus is put on its changes. Compared to the no-eddy experiment, the changes of the M₂ energy fluxes in the northern and southern part of the AE are opposite: increasing in the north and decreasing in the south (Fig. 5d). The most dramatic changes occur to the west of the eddy on the continental slope, decreasing to 15% of its original value or nearly doubling at some areas. However, the CE causes the M₂ energy fluxes to decrease in the eddy's northern half and near the southern edge but to increase in the remaining area (Fig. 5e). Changes on the continental slope are also more significant. Besides, the direction of the energy fluxes also changes, indicating that the M₂ ITs are refracted to the north by the AE and to the south by the CE.

4. Analysis of radiation rays and wave fronts

In this section, we will further explore the mechanism for refraction of the M₂ ITs by MEs based on propagation of energy radiating rays and wave front. The background current and stratification used in analysis are extracted from the corresponding idealized simulation (shown in Fig. 4).

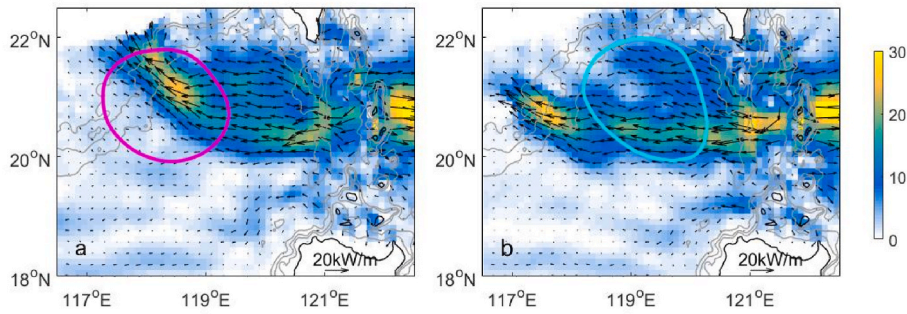Fig. 6 shows the theoretical energy radiating rays for the mode-1 M₂

Fig. 3. Depth-integrated baroclinic energy fluxes (quiver) and their magnitude (shading, unit: kW/m) of the M_2 ITs when encountering (a) an AE and (b) a CE. The magenta and cyan circles indicate locations of the AE and CE, respectively.
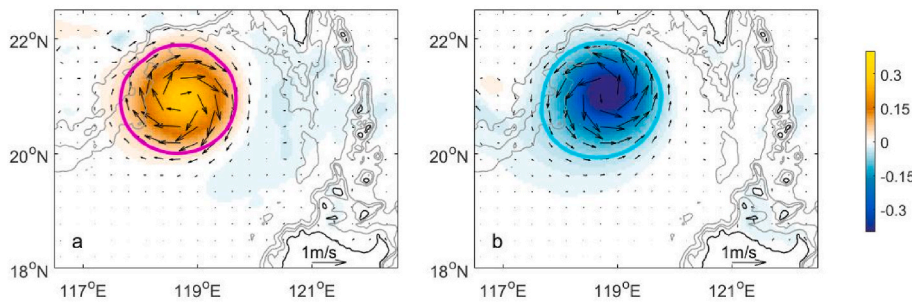

Fig. 4. Subtidal circulation on Day 11 in the (a) AE and (b) CE experiments with the surface elevation indicated by shadings (unit: m) and surface currents by arrows. The magenta and cyan circles indicate locations of the AE and CE, respectively.
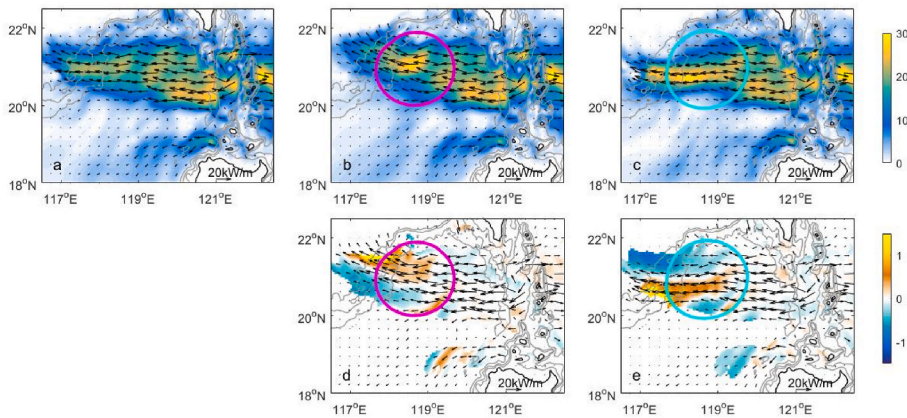

Fig. 5. Depth-integrated baroclinic energy fluxes (quiver) and their magnitude (shading, unit: kW/m) of the M_2 ITs in the (a) no-eddy, (b) AE, and (c) CE experiments. The relative changes of the energy flux magnitude in the (d) AE and (e) CE cases compared with the no-eddy case are also displayed, where only areas with magnitude greater than 5 kW/m are shown for clarity. The magenta and cyan circles indicate locations of the AE and CE, respectively.

ITs, which are calculated based on the ray-tracing model (Equation set (12); Duda et al., 2018). The CROCO simulated energy fluxes in idealized experiments are superposed for comparison. The ray trajectories follow the CROCO simulated energy flux vectors, although there is not one-to-one agreement because only the mode-1 westward propagating M_2 IT is considered in the theoretical model. When an AE exists to the west of the LS, the rays bifurcate near the southern edge of the eddy and the northern subbranch shows stronger refraction. However, the changes of ray trajectories within the CE are opposite to those within the AE: they become more convergent, focused within 20.5°N-21°N after passing the eddy center, which corresponds to the areas where energy fluxes increase in the CROCO simulation. It should be noted that, as the M_2 energy fluxes to the south of 20°N are fairly weak in the CROCO simulation, they show northward (southward) refraction by the AE (CE) rather than bifurcation (convergence) revealed by the ray tracing model

(Fig. 6a and d). Consider that both the background currents and stratification associated with MEs contribute to the refraction of ITs by changing the phase speed, we further compare their contribution. Fig. 6b (6e) show that AE- (CE-) induced changes in stratification result in refraction of rays but it is not obvious. On the contrary, in either the AE or the CE experiment, the changes in phase speed caused by currents have a significant influence on the ray trajectories (Fig. 6c and f). The AE causes most ray trajectories passing through the eddy to turn north and those passing by the southern edge to turn slightly south. The changes are opposite when a CE exists. In summary, the rays calculated with the currents-determined phase speed show a pattern more similar to those in Fig. 6a and d. In other words, the currents related to the eddies contribute more to the refraction of the M_2 IT than the stratification. This is consistent with the results of previous studies that background flow instead of stratification have a more significant influence on IT
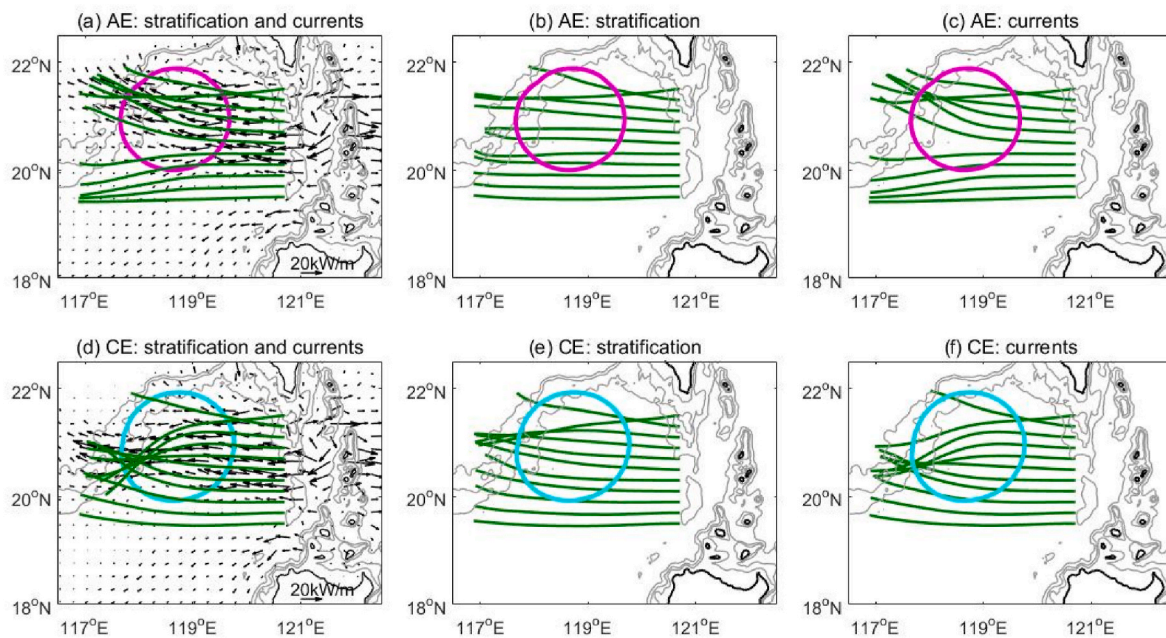
Fig. 6. M_2 IT ray trajectories (green lines) calculated with the background fields of the (a–c) AE and (d–f) CE experiments. During the calculation, the influence of stratification and currents is considered simultaneously in (a,d), but separately in (b,e) and (c,f), respectively. The depth-integrated energy fluxes of the M_2 IT in each experiment are shown by quivers in (a,d) for comparison. The magenta and cyan circles indicate locations of the AE and CE, respectively.
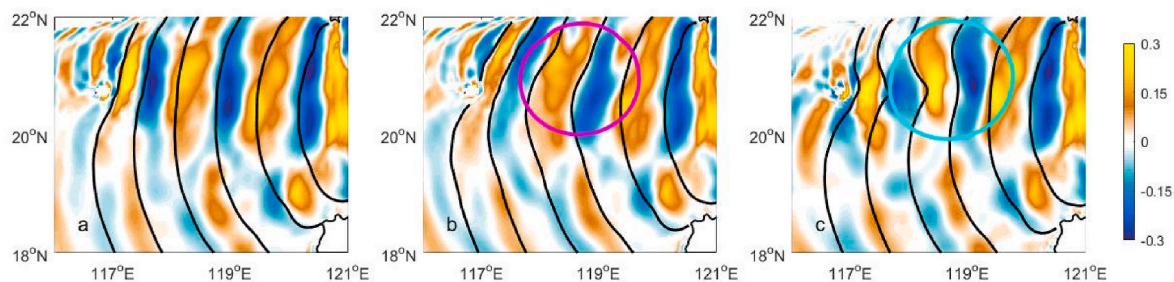

Fig. 7. Snapshots of the zonal velocity of the M_2 IT at 100 m depth (shadings, unit: m/s) and the wave front locations estimated from the empirical model (black lines) in the (a) no-eddy, (b) AE, and (c) CE experiments. The magenta and cyan circles indicate locations of the AE and CE, respectively.

refraction (Duda et al., 2018; Savage et al., 2020; Xu et al., 2021; Cao et al., 2022).

The mechanism of the M_2 IT refraction can be also confirmed by the empirical model for estimating the wave front (Jackson, 2009). In snapshots of the zonal velocity of the M_2 IT at 100 m depth, the 0 contours along the north branch of the M_2 westward energy fluxes show good agreement with the model wave fronts in terms of shape and orientation (Fig. 7). The AE causes convex of the wave front and the CE causes a concave pattern by changing the phase speed of the M_2 IT.

5. Summary and discussion

Background currents could change the generation and propagation of ITs. In the SCS, the Kuroshio, MEs and other subtidal currents are all intense and their impacts on ITs are hard to separate from each other. In this study, a pair of eddies successively passed the northern SCS were simulated in the realized experiment and results preliminarily indicated the modulation of IT by MEs. To further investigate the mechanism of IT refraction, we conducted idealized experiments, setting MEs on the main beam of the M_2 IT propagating from the LS into the SCS. The results show that the M_2 IT encountering an AE in its path would refract northward and a CE would cause refraction to the south. The refraction leads to significant changes of the M_2 energy flux on the continental

slope besides within the eddy. The CROCO simulation shows good agreement with model ray trajectories and wave fronts locations, indicating that the MEs cause refraction of the M_2 IT by changing the phase speed field. Based on the raying-tracing model, we find that the background currents related to the MEs contribute more to the refraction than the stratification.

The role of subtidal circulation on internal waves has been discussed in previous studies. However, focus has been mainly put on the Kuroshio with different paths (Jan et al., 2012; Xie et al., 2021; Xu et al., 2021; Cao et al., 2022). This study makes an attempt to investigate the impacts of MEs on IT propagation separately from that of other subtidal circulation. The results have important implications for investigation of spatial and temporal variations in the magnitude and direction of the M_2 IT energy fluxes. In addition, since the formation of internal solitary waves is related to the semidiurnal ITs via nonlinear steeping process (Helfrich and Grimshaw, 2008; Cai et al., 2012), refraction of the M_2 IT by the eddies has great implication for internal solitary waves prediction (Park and Farmer, 2013; Li et al., 2016). Impacts of eddies with different location and intensity may be further quantified in future studies.

Declaration of competing interest

The authors declare that they have no known competing financial

interests or personal relationships that could have appeared to influence the work reported in this paper.

Data availability

Acknowledgements

Appendix A. Supplementary data

Supplementary data to this article can be found online at https://doi.org/10.1016/j.dsr.2022.103946.

References

Alford, M.H., Peacock, T., MacKinnon, J.A., Nash, J.D., Buijsman, M.C., Centurioni, L.R., Fringer, O.B., 2015. The formation and fate of internal waves in the South China Sea. Nature 521 (7550), 65.

Cai, S., Xie, J., He, J., 2012. An overview of internal solitary waves in the South China sea. Surv. Geophys. 33 (5), 927–943. https://doi.org/10.1007/s10712-012-9176-0.

Cao, A.-Z., Li, B.-T., Lv, X.-Q., 2015. Extraction of internal tidal currents and reconstruction of full-depth tidal currents from mooring observations. J. Atmos. Ocean. Technol. 32 (7), 1414–1424.

Cao, A., Guo, Z., Wang, S., Guo, X., Song, J., 2022. Incoherence of the M2 and K1 internal tides radiated from the Luzon Strait under the influence of looping and leaping Kuroshio. Prog. Oceanogr. 206, 102850 https://doi.org/10.1016/j.pocean.2022.102850.

Chavanne, C., Flament, P., Carter, G., Merrifield, M., Luther, D., Zaron, E., Gurgel, K.W., 2010. The surface expression of semidiurnal internal tides near a strong source at Hawaii. Part I: observations and numerical predictions. J. Phys. Oceanogr. 40 (6), 1155–1179.

Chen, G., Hou, Y., Chu, X., 2011. MEs in the South China Sea: mean properties, spatiotemporal variability, and impact on thermohaline structure. J. Geophys. Res.: Oceans 116 (C6).

Duda, T.F., Lin, Y.-T., Buijsman, M., Newhall, A.E., 2018. Internal tidal modal ray refraction and energy ducting in baroclinic gulf stream currents. J. Phys. Oceanogr. 48 (9), 1969–1993.

Dunphy, M., Lamb, K.G., 2014. Focusing and vertical mode scattering of the first mode internal tide by mesoscale eddy interaction. J. Geophys. Res.: Oceans 119 (1), 523–536.

Egbert, G.D., Erofeeva, S.Y., 2002. Efficient inverse modeling of barotropic ocean tides. J. Atmos. Ocean. Technol. 19 (2), 183–204.

Garrett, C., Kunze, E., 2007. Internal tide generation in the deep ocean. Annu. Rev. Fluid Mech. 39, 57–87.

Guo, Z., Cao, A., Lv, X., Song, J., 2020a. Impact of multiple tidal forcing on the simulation of the M2 internal tides in the northern South China Sea. Ocean Dynam. 70 (2), 187–198.

Guo, Z., Cao, A., Lv, X., Song, J., 2020b. Impacts of stratification variation on the M2 internal tide generation in Luzon Strait. Atmos.-Ocean 58 (3), 206–218.

Guo, Z., Cao, A., Wang, S., 2021. Influence of remote internal tides on the locally generated internal tides upon the continental slope in the South China sea. J. Mar. Sci. Eng. 9 (11), 1268.

Helfrich, K.R., Grimshaw, R.H.J., 2008. Nonlinear disintegration of the internal tide. J. Phys. Oceanogr. 38 (3), 686–701. https://doi.org/10.1175/2007jpo3826.1.

Huang, X., Wang, Z., Zhang, Z., Yang, Y., Zhou, C., Yang, Q., Tian, J., 2018. Role of MEs in modulating the semidiurnal internal tide: observation results in the northern South China sea. J. Phys. Oceanogr. 48 (8), 1749–1770.

Jackson, C.R., 2009. An empirical model for estimating the geographic location of nonlinear internal solitary waves. J. Atmos. Ocean. Technol. 26 (10), 2243–2255.

Jan, S., Chern, C.S., Wang, J., Chiou, M.D., 2012. Generation and propagation of baroclinic tides modified by the Kuroshio in the Luzon Strait. J. Geophys. Res.: Oceans 117 (C2).

Kerry, C.G., Powell, B.S., Carter, G.S., 2013. Effects of remote generation sites on model estimates ofM2Internal tides in the philippine sea. J. Phys. Oceanogr. 43 (1), 120927134059000.

Kerry, C.G., Powell, B.S., Carter, G.S., 2014. The impact of subtidal circulation on internal tide generation and propagation in the Philippine Sea. J. Phys. Oceanogr. 44 (5), 1386–1405.

Kerry, C.G., Powell, B.S., Carter, G.S., 2016. Quantifying the incoherent M2 internal tide in the Philippine Sea. J. Phys. Oceanogr. 46 (8), 2483–2491.

Large, W.G., McWilliams, J.C., Doney, S.C., 1994. Oceanic vertical mixing: a review and a model with a nonlocal boundary layer parameterization. Rev. Geophys. 32 (4), 363–403.

Li, Q., Wang, B., Chen, X., Chen, X., Park, J.-H., 2016. Variability of nonlinear internal waves in the South China Sea affected by the Kuroshio and mesoscale eddies. J. Geophys. Res.: Oceans 121 (4), 2098–2118. https://doi.org/10.1002/2015JC011134.

Liang, X., 2014. Semidiurnal tidal currents in the deep ocean near the East Pacific Rise between 9° and 10°N. J. Geophys. Res.: Oceans 119 (7), 4264–4277. https://doi.org/10.1002/2013JC009522.

Löb, J., Köhler, J., Mertens, C., Walter, M., Li, Z., von Storch, J.-S., Rhein, M., 2020. Observations of the low-mode internal tide and its interaction with mesoscale flow south of the azores. J. Geophys. Res.: Oceans 125 (11), e2019JC015879. https://doi.org/10.1029/2019JC015879.

Marchesiello, P., Nguyen, N.M., Gratiot, N., Loisel, H., Anthony, E.J., Dinh, C.S., Kestenare, E., 2019. Erosion of the coastal Mekong delta: assessing natural against man induced processes. Continent. Shelf Res. 181, 72–89. https://doi.org/10.1016/j.csr.2019.05.004.

Michael Dunphy, 2014. Focusing and Vertical Mode Scattering of the First Mode Internal Tide via Mesoscale Eddy Interactions. Doctoral dissertation, University of Waterloo, Waterloo, Canada). Retrieved from. http://hdl.handle.net/10012/8865.

Nagai, T., Saito, H., Suzuki, K., Takahashi, M., 2019. Kuroshio Current: Physical, Biogeochemical, and Ecosystem Dynamics, vol. 243. John Wiley & Sons.

Nash, J.D., Alford, M.H., Kunze, E., 2005. Estimating internal wave energy fluxes in the ocean. J. Atmos. Ocean. Technol. 22 (10), 1551–1570.

NOAA National Geophysical Data Center. 2009: ETOPO1 1 Arc-Minute Global Relief Model. NOAA National Centers for Environmental Information.

Park, J.-H., Farmer, D., 2013. Effects of Kuroshio intrusions on nonlinear internal waves in the South China Sea during winter. J. Geophys. Res.: Oceans 118 (12), 7081–7094. https://doi.org/10.1002/2013JC008983.

Ponte, A.L., Klein, P., 2015. Incoherent signature of internal tides on sea level in idealized numerical simulations. Geophys. Res. Lett. 42 (5), 1520–1526. https://doi.org/10.1002/2014GL062583.

Rainville, L., Pinkel, R., 2006. Propagation of low-mode internal waves through the ocean. J. Phys. Oceanogr. 36 (6), 1220–1236.

Renault, L., McWilliams, J.C., Penven, P., 2017. Modulation of the agulhas current retroflection and leakage by oceanic current interaction with the atmosphere in coupled simulations. J. Phys. Oceanogr. 47 (8), 2077–2100. https://doi.org/10.1175/jpo-d-16-0168.1.

Rudnick, D.L., Boyd, T.J., Brainard, R.E., Sanford, T.B., 2003. From tides to mixing along the Hawaiian ridge. Science 301, 355–357. https://doi.org/10.1126/science.1085837.

Rudnick, D.L., Jan, S., Centurioni, L., Lee, C.M., Lien, R.-C., Wang, J., Chern, C.-S., 2011. Seasonal and mesoscale variability of the Kuroshio near its origin. Oceanography 24 (4), 52–63.

Savage, A.C., Waterhouse, A.F., Kelly, S.M., 2020. Internal tide nonstationarity and wave–mesoscale interactions in the tasman sea. J. Phys. Oceanogr. 50 (10), 2931–2951. https://doi.org/10.1175/jpo-d-19-0283.1.

Song, P., Chen, X., 2020. Investigation of the internal tides in the northwest pacific ocean considering the background circulation and stratification. J. Phys. Oceanogr. 50 (11), 3165–3188. https://doi.org/10.1175/jpo-d-19-0177.1.

Varlamov, S.M., Guo, X., Miyama, T., Ichikawa, K., Waseda, T., Miyazawa, Y., 2015. M2 baroclinic tide variability modulated by the ocean circulation south of Japan. J. Geophys. Res.: Oceans 120 (5), 3681–3710. https://doi.org/10.1002/2015JC010739.

Wagner, G., Ferrando, G., Young, W., 2017. An asymptotic model for the propagation of oceanic internal tides through quasi-geostrophic flow. J. Fluid Mech. 828, 779–811. https://doi.org/10.1017/jfm.2017.509.

Wang, S., Cao, A., Li, Q., Chen, X., 2021. Reflection of K1 internal tides at the continental slope in the northern South China sea. J. Geophys. Res.: Oceans 126 (7), e2021JC017260. https://doi.org/10.1029/2021JC017260.

Xie, J., He, Y., Chen, Z., Xu, J., Cai, S., 2015. Simulations of internal solitary wave interactions with mesoscale eddies in the northeastern south China sea. J. Phys. Oceanogr. 45 (12), 2959–2978. https://doi.org/10.1175/jpo-d-15-0029.1.

Xie, J., Fang, W., He, Y., Chen, Z., Liu, G., Gong, Y., Cai, S., 2021. Variation of internal solitary wave propagation induced by the typical oceanic circulation patterns in the northern South China sea deep basin. Geophys. Res. Lett. 48 (15), e2021GL093969 https://doi.org/10.1029/2021GL093969.

Xu, Z., Liu, K., Yin, B., Zhao, Z., Wang, Y., Li, Q., 2016. Long-range propagation and associated variability of internal tides in the South China Sea. J. Geophys. Res.: Oceans 121 (11), 8268–8286.

Xu, Z., Wang, Y., Liu, Z., McWilliams, J.C., Gan, J., 2021. Insight into the dynamics of the radiating internal tide associated with the Kuroshio current. J. Geophys. Res.: Oceans 126 (6), e2020JC017018. https://doi.org/10.1029/2020JC017018.

Zaron, E.D., Egbert, G.D., 2014. Time-variable refraction of the internal tide at the Hawaiian Ridge. J. Phys. Oceanogr. 44 (2), 538–557.

Zhang, Z., Zhao, W., Tian, J., Liang, X., 2013. A mesoscale eddy pair southwest of Taiwan and its influence on deep circulation. J. Geophys. Res.: Oceans 118 (12), 6479–6494. https://doi.org/10.1002/2013JC008994.

Zhang, Z., Tian, J., Qiu, B., Zhao, W., Chang, P., Wu, D., Wan, X., 2016. Observed 3D structure, generation, and dissipation of oceanic MEs in the South China Sea. Sci. Rep. 6, 24–349. https://doi.org/10.1038/srep24349.

Zhao, Z., 2014. Internal tide radiation from the Luzon Strait. J. Geophys. Res.: Oceans 119 (8), 5434–5448.

Zhao, Z., 2020. Southward internal tides in the northeastern south China sea. J. Geophys. Res.: Oceans 125 (11), e2020JC016554. https://doi.org/10.1029/2020JC016554.

Zhao, Z., Alford, M.H., MacKinnon, J.A., Pinkel, R., 2010. Long-range propagation of the semidiurnal internal tide from the Hawaiian ridge. J. Phys. Oceanogr. 40 (4), 713–736.

Zilberman, N., Merrifield, M., Carter, G., Luther, D., Levine, M., Boyd, T., 2011. Incoherent nature of M 2 internal tides at the Hawaiian Ridge. J. Phys. Oceanogr. 41 (11), 2021–2036.